Journal of the European Ceramic Society 17 (1997) 495–504

PII: S0955-2219(96)00099-4
0955-2219/97/$17.00

The Toughening of Alumina with Iron: Effects of Iron Distribution on Fracture Toughness

P. A. Trusty* & J. A. Yeomans

Department of Materials Science and Engineering, University of Surrey, Guildford, Surrey GU2 5XH, UK

(Received 1 May 1996; revised version received 22 May 1996; accepted 30 May 1996)

Abstract

Two composites have been fabricated by hot pressing powder blends of alumina with 20 volume percent of ductile iron particles. The composites differ in the shape, size and distribution of the iron particles. The fracture toughness of each composite has been obtained in situ, *by testing inside a scanning electron microscope, using a double cantilever beam technique modified specifically for small ceramic specimens. Observation of the crack–particle interactions has enabled information to be gained about the toughening mechanisms occurring and hence the parameters for microstructural tailoring of these materials have been deduced. Results showed that the fracture toughness of the composites differed greatly due to the distribution of the iron throughout the microstructure, which in turn affected the type and degree of observed toughening mechanism. These material-specific toughening parameters were then used to fabricate a third alumina/iron composite with a more optimised fracture toughness.* © *1997 Elsevier Science Limited. All rights reserved.*

1 Introduction

The inherent brittle nature of ceramic materials is a disadvantage when considering their use in engineering applications. It has been established that the incorporation of a metallic second phase into a brittle ceramic matrix can produce a tougher material without reducing substantially the dominant properties of the ceramic. The main potential toughening characteristic imparted by a metallic second phase is the dissipation of energy by plastic deformation. The magnitude of toughness increase is related directly to the ability of the ductile particles to deform plastically, span the faces of a propagating crack and impose closure tractions which reduce the stress intensity at the crack tip. If the bridging reinforcements do not fail immediately on crack interception, the increasing resistance to crack propagation which results is known as K_R-curve behaviour. Examples of brittle/ductile systems which have been studied to date include glass/lead;[1] glass/Ni;[2] alumina/aluminium;[3] alumina/nickel;[4,5] alumina/iron.[6] Theoretical work suggests that the fracture toughness of the composites depends on factors such as the volume fraction and yield strength of the metallic phase, and the bridging length prior to ductile failure.[7–9]

Experimental work has shown that the mechanism of plastic deformation is likely to occur with ductile secondary phases which are continuous fibres,[10] boundary networks,[11] or foils,[12] as there is forced crack/secondary phase interaction due to the shape of the ductile phase in these cases. For composites which are reinforced with a discontinuous particulate phase, however, the studies which have been undertaken have shown that in some cases there was a positive toughening increment on crack–particle interaction,[13,14] whilst in others there was not.[2,15] The latter cases occurred when matrix cracks were not attracted to the ductile particles due to unfavourable residual stress and Young's modulus mismatch conditions. When considering a particulate second phase, therefore, the dominant toughening mechanism may not be plastic deformation, but may be another mechanism, for example, crack branching or crack bridging.[16,17] In addition, the morphology/distribution of the secondary phase throughout the ceramic matrix can affect significantly the type and abundance of toughening mechanisms which occur. If these mechanisms can be observed directly, subsequent predictions, based on experimental evidence, can be made to optimise the fracture toughness for the particular composite system.

*Present address: Interdisciplinary Research Centre in Materials for High Performance Applications, The University of Birmingham, Birmingham B15 2TT, UK.

This study investigates the toughening mechanisms occurring in ductile iron particle-reinforced alumina matrix composites. The *in situ* nature of the testing technique employed enables the toughening mechanisms to be observed directly and compared with those assumed by theory. By analysis of the data from two morphologically different alumina/iron composites, the characteristics required for a material with a more optimised fracture toughness are determined and a third alumina/iron composite material is fabricated and analysed.

2 Experimental Procedure

2.1 Material fabrication

Composite powder blends were mixed from alumina powder (nominal particle size 0·4 μm, AKP-30, Sumitomo Chemical Company, Japan) and iron powder (nominal particle size 8 μm, H. C. Starck, Dusseldorf) to give 20% by volume of iron and then dry milled in polypropylene bottles for 4 h to ensure thorough mixing. Small cylindrical alumina milling media were added to the blend to aid the mixing process and break up any alumina agglomerations that were present.

For a more homogeneous distribution of iron in alumina it was necessary to alter the powder processing route. Powders were mixed in the same proportions as described above, but in order to reduce the propensity for alumina agglomerations, isopropanol was added to the blend to make a slurry. This slurry was milled for 8 h in a polypropylene bottle with alumina milling media and then dried in oven at a temperature of 30°C for 12 h. The resultant powder was then crushed with a porcelain pestle to give an assortment of powder blend agglomerations, each agglomeration containing a discrete distribution of iron particles in alumina.

Batches of the powder blends (25 g) were placed in a cylindrical graphite die of internal diameter 25 mm and heated to a temperature of 1400°C at a rate of 20°C min. The die was prevented from oxidising by an inert argon atmosphere. At temperature, a uniaxial pressure of 25 MPa was applied. Both pressure and temperature were held for a period of 30 min and then the whole configuration was left to cool to room temperature. The composite material fabricated from the wet-milled blend is designated as Composite A and the composite fabricated from the dry-milled blend is designated Composite B. Monolithic alumina specimens were prepared also for comparative purposes.

2.2 Material characterisation

Characterisation of the composite materials was undertaken by conventional density measurements based on Archimedes' principle and the use of X-ray diffractometry (XRD), reflected light microscopy (RLM) and scanning electron microscopy (SEM) techniques.

The main mechanical property of interest for these materials was the fracture toughness of each composite. The technique employed for the measurement of fracture toughness was the double cantilever beam (DCB) method. For a uniform DCB specimen, the strain energy release rate is dependent on crack length. Use of a correctly tapered specimen[18] can create a situation in which the compliance is independent of crack length, but the machining of such specimens is especially difficult when considering small ceramic specimens. Hence, a DCB testing technique was developed specifically for this study to allow observations of crack–particle interaction mechanisms. These mechanisms are important in determining the relationship between microstructure and fracture toughness.

The initial experimental specimen configuration for this test was a rectangular plate of dimensions 22 mm in length, 12 mm wide and 2 mm thick. The specimen was grooved on both sides (*c.*0·5 mm in depth) in order to guide the advancing crack and to retain the mode I opening of the traditional double cantilever beam specimen.[19] In order to be able to observe the advancing crack, the groove was polished to a 1 μm finish using several grades of diamond paste and an air tool fitted with a brass ring (10 mm diameter × 1 mm thick). The loading of the DCB specimen was made possible by attaching brass end tags to one end of the specimen using a high temperature curing adhesive (Permabond ESP 105T). Before the DCB tests could commence, a crack initiation point was required. This was achieved by machining a notch into the grooved portion of a specimen (notch thickness 0·4 mm). The specimen was tilted in relation to the blade used to machine this notch so that an angled notch was cut. This tapered notch assisted in the crack initiation by supplying a thin wedge of material from which the crack could initiate and grow until it reached the full through-thickness of the specimen. This technique avoids the more time-consuming indentation notching technique employed by Rôdel *et al.*[20]

The *in situ* testing of the DCB specimens was achieved through use of the straining stage which was placed inside the chamber of a Cambridge S100 scanning electron microscope. The motor speed, and the data logging were controlled externally via computer. A typical test procedure commenced by fixing a gold-coated DCB specimen to the central fixture of the straining stage. The stage

was positioned inside the chamber of the SEM in such a way as to optimise the working distance between the electron beam and the specimen (approximately 10 mm).[19] On evacuating the chamber, the initial notch tip was positioned such that a crack could be followed as it grew horizontally from left to right. The specimen was loaded to the point of crack initiation at a cross-head speed of 0·03 mm/min. This speed was used to reduce the probability of catastrophic failure via unstable crack propagation following Vekinis *et al.*[21] The crack opening and propagation were then monitored by stopping the motor after each crack propagation step and measuring the length of crack and the corresponding load. Any salient crack–particle interactions were also photographed throughout the test.

After specimen failure, the results obtained were used to generate K_R-curves. For the DCB test, K_R-curve data were calculated using a modified form of the equation developed for a standard test specimen which accounts for the central groove in the test specimen.[19] There were two main assumptions that were made when calculating the fracture toughness data. The crack length was measured from the centre of the loading pins and the slight bending moment present in the brass end-tags was assumed to have a negligible effect on the load/crack measurements during testing.

3 Results and Discussion

3.1 Fracture toughness

This section will first compare the fracture toughness properties of Composites A and B, and then describe Composite C, a composite in which the microstructure has been tailored to optimise toughness as a consequence of the data acquired from A and B.

Reflected light photomicrographs of Composites A and B, which show the differences in microstructures, are shown in Fig. 1. As can be seen, Composite A contains a discrete dispersion of iron particles throughout the alumina matrix, whereas Composite B has a more 'honeycombed' appearance in which iron particles are situated around the edges of large alumina regions. The results of the DCB experiments for the monolithic material and both composites are summarised in Table 1. Example K_R-curves obtained by DCB testing are shown in Fig. 2. Stable crack growth conditions could not be achieved in the monolithic alumina and a single mean value of 3·3 MPa $m^{1/2}$ was recorded (with a standard deviation of 0·16 MPa $m^{1/2}$ which indicates good reproducibility). As stable crack growth did not occur, it was not possible to observe any energy-dissipating mechanisms during fracture. The results in Table 1 show that for both composites, the addition of a ductile phase to alumina leads to a tougher material. There is, however, a marked difference in the toughness values of the composites and the shapes of the K_R-curves, indicating that the two composites are behaving differently.

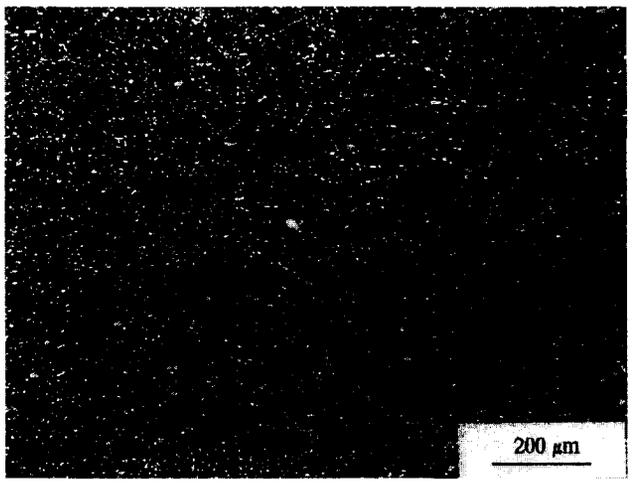

(a)

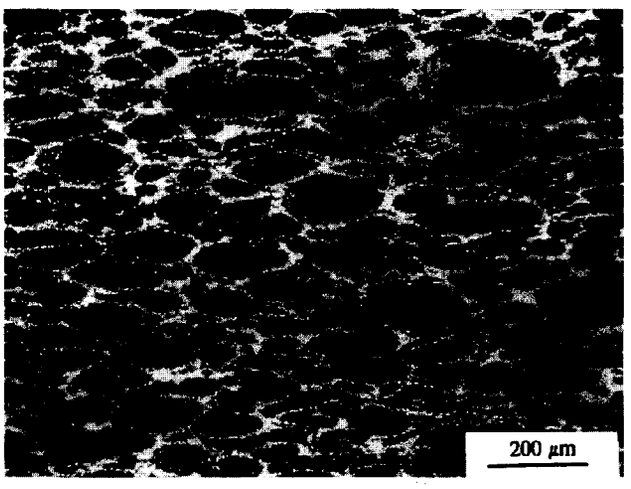

(b)

Fig. 1. Reflected light photomicrographs of (a) Composite A and (b) Composite B.

Table 1. Results of the double cantilever beam tests of Composites A and B

Specimen	*Plateau K_c (Mpa $m^{1/2}$)*	*Mean K_c (Mpa $m^{1/2}$)*	*ΔK/MPa $m^{1/2}$ (% increase)*	*Process zone length (mm)*
Alumina	3·2 3·5 3·1	3·3	—	—
Composite A	6·4 6·6 6·7	6·6	3·3 (100)	5·4
Composite B	10·7 9·8 10·0	10·2	6·9 (209)	4·5

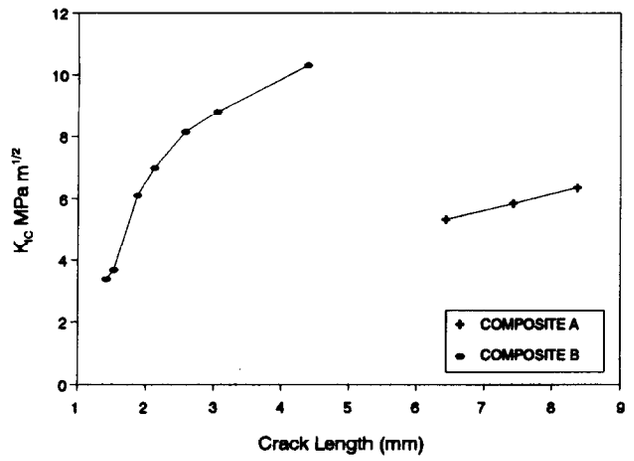

Fig. 2 . Example K_R-curves from the double cantilever beam testing of Composites A and B.

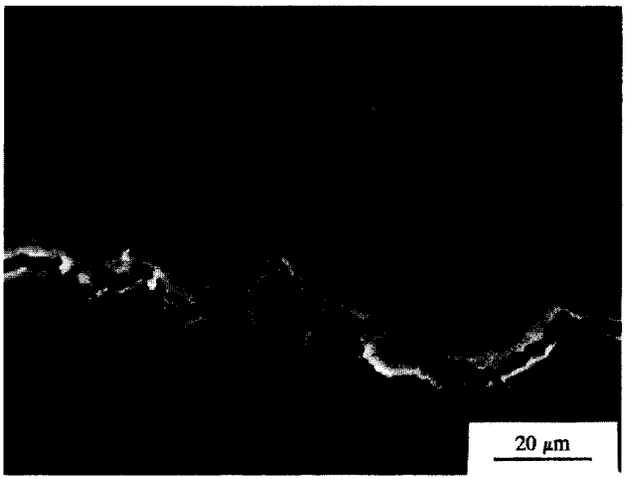

(a)

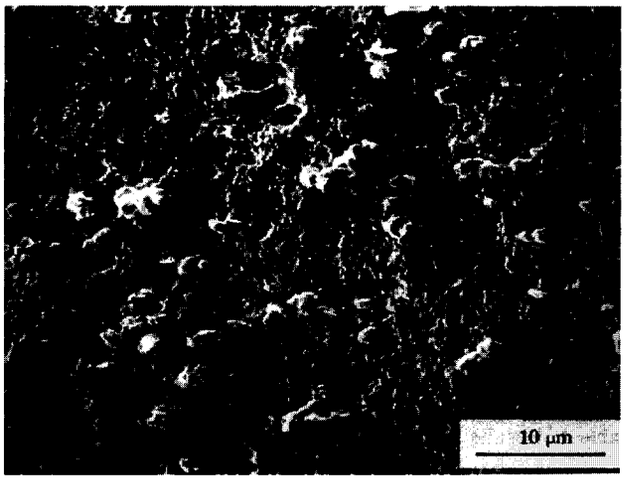

(b)

Fig. 3. Scanning electron photomicrographs of typical crack–particle interactions in Composite A. (a) Side view showing the crack following the particle–matrix interface. (b) Fracture surface showing intact iron particles and cavities formed due to pullout.

Reference to the K_R-curves for Composite A show that there is only a relatively small increase in toughness with crack length and the relationship appears to be linear. It should be noted also that a crack length of over 6 mm was required

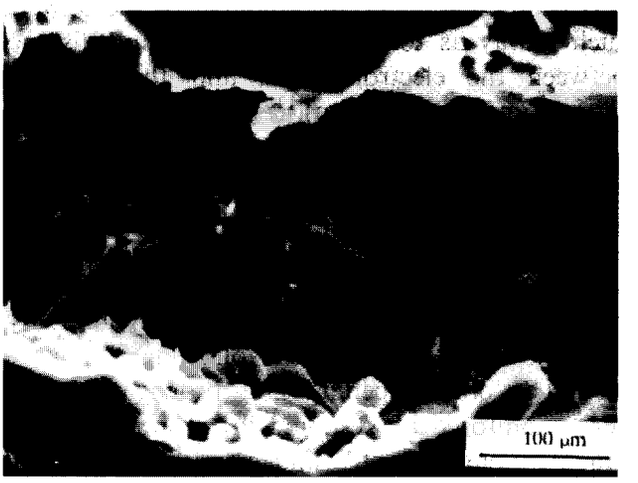

Fig. 4. Scanning electron photomicrograph showing an iron particle that has deformed plastically on crack interaction, and subsequently stretched to failure.

prior to the first point on the curve indicating that the data for the initial rising region of the K_R-curve have been lost due to unstable crack-propagation conditions. Study of the crack–particle interactions in this composite shows that debonding along the alumina–iron interface was the dominant crack tip shielding mechanism, with less than 2% of the iron particles deforming plastically. Figure 3 shows a typical crack propagation route through Composite A and specimen fracture surface. Iron particles can be seen that are still attached to the matrix, but there are also cavity sites where iron particles have been pulled free. This is indicative of the weak interfacial bond. In Composite A, it would appear that the increase in toughness is a result of crack tip deflection on interaction with the iron phase. This leads to crack faces that are rougher than those observed in the monolithic alumina. Dissipation of energy by frictional interaction may occur as the faces separate.

The shape of the K_R-curve of Composite B differs from that of Composite A in the early stages of crack growth, indicating that the material is behaving in a different manner. Observation of the crack particle interactions in Composite B showed that as many as 30% of the iron agglomerations had deformed plastically. It should be noted that the plastic deformation of the particles is not the classical ligament stretching that is assumed to be occurring when the potential toughening increment is predicted according to the theory of Ashby *et al.*[1] Instead, the particles shear and the iron behaves like a hinge, bridging the crack faces.

In Composite B it would appear that it is not energetically favourable for the crack to follow the alumina–iron interface in every case, in con-

Fig. 5. Computer-generated schematic reconstruction of the surface roughness in Composites A and B. (The data were collated from experimental observations).

trast to the behaviour of Composite A. Debonding is occurring in Composite B and will contribute to the toughening increment, but the data indicate that there is a significant contribution also from the plastic deformation of the iron (Fig. 4). It is not unreasonable to assume that the interfacial bond strength is similar in A and B because they were fabricated under identical conditions. Hence, the differences in the crack–particle interactions can be attributed to the differences in the shape and distribution of the iron in the two composites. The iron in Composite B is agglomerated and of a more irregular shape than in Composite A, decreasing the propensity for debonding and encouraging plastic deformation. This, coupled with greater crack deflection if debonding does occur, leads to greater toughening increments and rougher fracture surfaces than those observed in Composite A.

3.2 Crack profiles

The roughness of the post-failure specimens is shown in a quantitative manner for Composites A and B in Fig. 5. The collated data used to recreate these profiles can be displayed in terms of the angular deviation of the crack as it traverses the specimen and the length of each crack segment prior to deviation. Histograms depicting these phenomena are shown in Fig. 6. Considering the length distribution of Composite A, it can be seen that the most frequent distance traversed prior to crack deviation was in the 0–64 μm region. In the majority of cases the iron particles were the cause of crack meandering due to the weak interface being a preferential crack propagation site (Fig. 3). Hence, the high frequency of the short propagation distances in Composite A is due to the closeness and abundance of the iron particles.

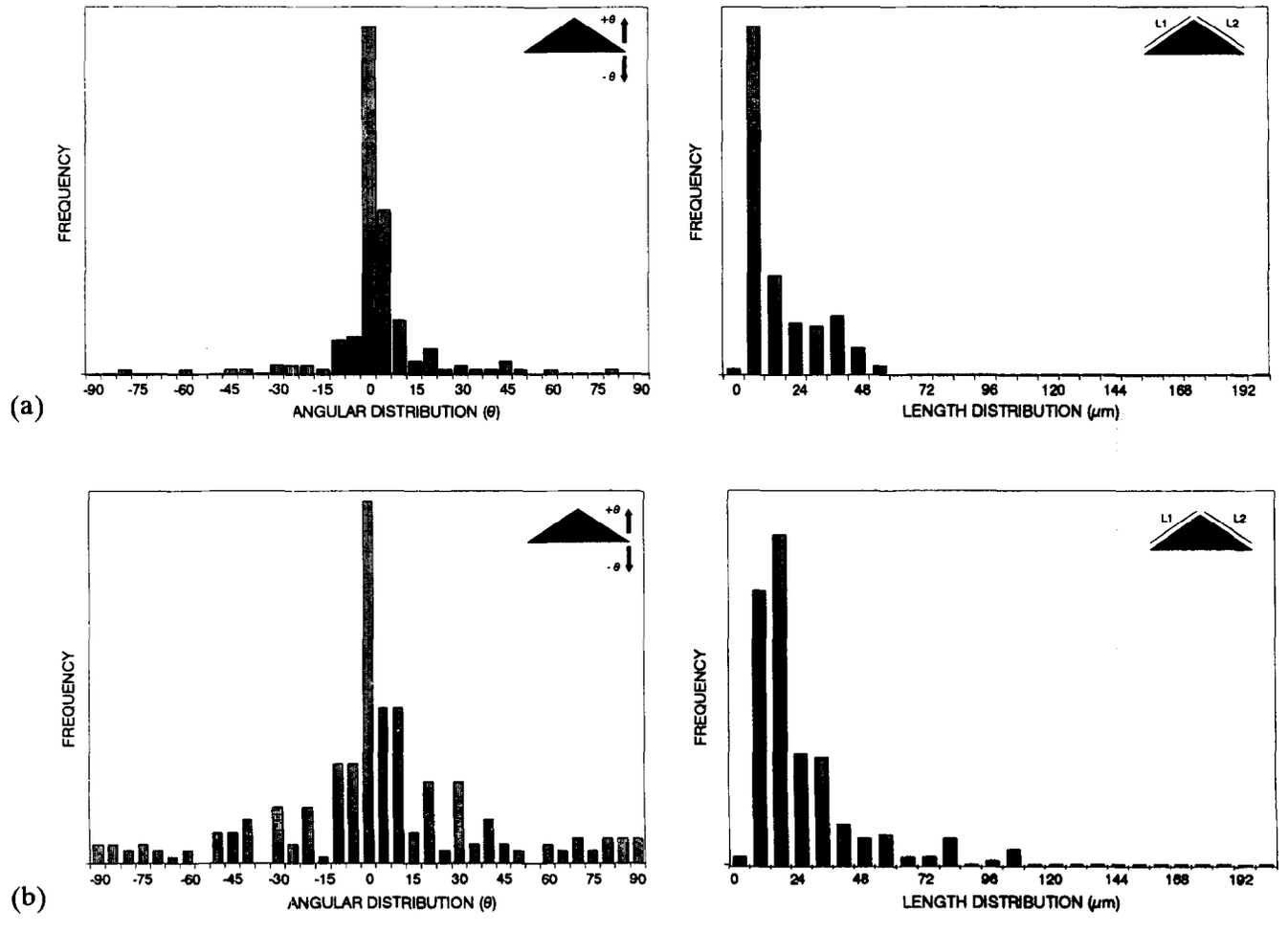

Fig. 6. Histograms depicting the length and angular distributions which describe the crack paths in (a) Composite A and (b) Composite B. Note each unit of length corresponds to 8 μm.

Although there were many short propagation distances prior to deviation in Composite A, Fig. 6(b) shows that the most frequent angle of deviation was between 0 and 5°. The shallow angles were a direct result of the size and shape of the iron phase. The small and comparatively regular particles produce deviations which scale with the particle diameter, and the propensity for sharp re-entrant angles (high angle deviations), is low due to the regular shape (approximately spherical) of the iron.

The length distribution histogram of Composite B (Fig. 6(c)) has an overall shape which is different to that of Composite A. This difference can be attributed to the difference in the distribution of the iron and alumina in Composite B. The propagating crack is able to traverse the large alumina-rich regions with minimal deviation and may travel for some distance along the interface of a large iron agglomeration. These phenomena caused the 64–128 μm crack length range to be the most frequent in this composite.

Considering the angular deviations in Composite B (Fig. 6(d)), the overall shape of this histogram is different to the angular distribution of that of Composite A. The crack front meandering is again attributed to the preferential propagation site of the interface, but due to the irregular shape of the iron agglomerations, the angular deviations are far more pronounced than with Composite A. It is interesting to note the abundance of angular deviations in the 10–45° region. Deviations of this order and above are far more likely to correspond to mechanical interlocking of the iron phase between separating crack faces and frictional bridging.

The data collated from the crack path profiles of post-failure DCB specimens enable a comparison to be made between different materials. An ideal crack profile would be one which contained many short crack propagation lengths which had high angles of deviation. In this way, the probability of mechanical interlocking and, hence, crack tip shielding is increased leading to a more steeply rising K_R curve. The short crack propagation lengths are a feature of Composite A, whereas higher deviation angles are exhibited by Composite B. This suggests that a material with a microstructure which contained elements of both Composites A and B may produce a more ideal profile. It should be noted that for a different ductile-brittle system, other toughening mechanisms may be in effect[22] which would lead to a different microstructural optimisation prediction at this stage.

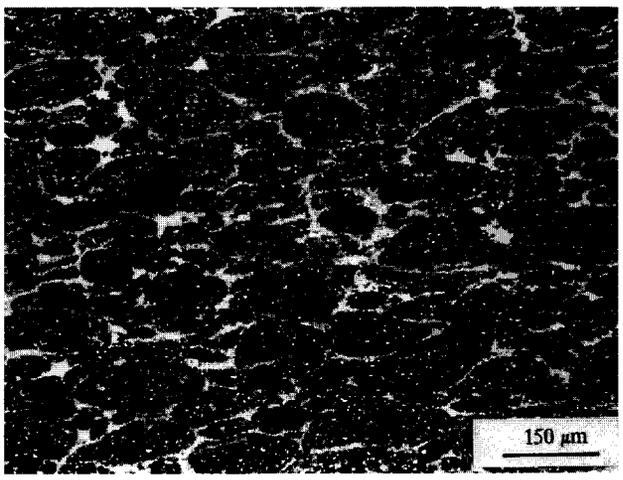

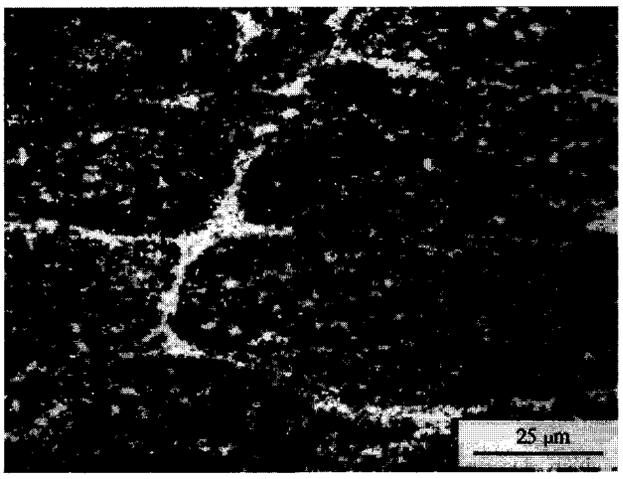

Fig. 7. Reflected light photomicrographs of Composite C.

3.3 Fabrication and properties of 'tailored' Composite C

3.3.1 Powder processing

Alumina (200 g) was weighed out into a container. The amount of iron required to give 20% by volume in alumina was weighed out also and divided into two equal batches. The first batch of iron was then dry milled with the alumina. This powder blend was then wet milled in isopropanol for a period of 8 h, and dried in an oven at 30°C. The resultant powder was sieved in order to ensure that there were no powder agglomerations greater than 150 μm. Pure iron (batch 2) was then added to this dried powder blend and dry milled for 4 h. Hot pressing of this powder mixture was performed using the same procedure as used for Composites A and B. Hence, the fabricated composite material (hereafter known as Composite C) contained 20% by volume of iron particles in an alumina matrix.

3.3.2 Preliminary microstructural characterisation

Figure 7 shows a reflected light photomicrograph of Composite C. Like Composite B, Composite C has a microstructure which is network in appearance and contains a degree of anisotropy caused by the hot pressing procedure. The iron regions which make up the networked regions in Composite

Table 2. Results of the double cantilever beam tests of Composite C

Specimen	*Plateau K_c (MPa $m^{1/2}$)*	*Mean K_c (MPa $m^{1/2}$)*	*ΔK/MPa $m^{1/2}$ (% increase)*	*Process zone length (mm)*
Composite C	10·8 10·6 11·2	10·9	7·6 (230)	6·5

C, however, are thinner than those in Composite B. This is because the network in Composite C is formed from only 10% by volume of iron as opposed to 20% by volume as with Composite B. The remaining 10% of iron in Composite C is evenly distributed in the equivalent of the alumina-rich regions in Composite B. Hence, the microstructure of Composite C contains elements of Composites A and B.

Composite C was tested using DCB and the average plateau fracture toughness value from this test was 10·90 MPa $m^{1/2}$ (see Table 2). This value is higher than that for both Composites A and B and hence, by combining elements from Composites A and B, a tougher composite has been produced. The K_R-curve of Composite C is shown in Fig. 8. This curve appears to be linear although it is noted that the first point occurs at a crack increment of 4·1 mm and, therefore, the data from the initial rising part of the curve have been lost due to unstable crack propagation conditions. The data which comprise this linear region of the K_R-curve, however, imply that debonding was the predominant energy-dissipating mechanism, due to the shallow gradient of the curve in this region.[23]

The crack–particle interactions were observed and recorded during the DCB test and examples are shown in Fig. 9. From these photomicrographs, it can be seen that, as with Composites A and B, the crack followed the interface between the iron and alumina. It should be noted also that

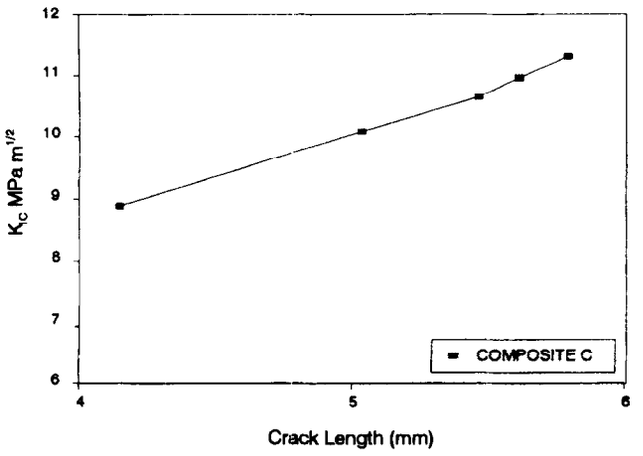

Fig. 8. An example K_R-curve from the double cantilever beam testing of Composite C.

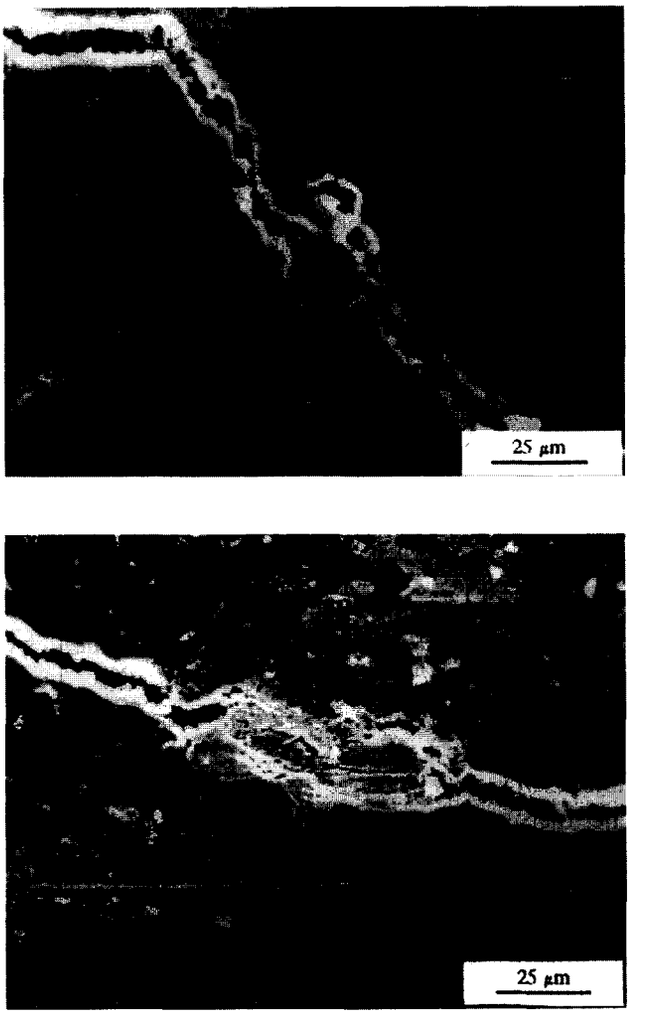

Fig. 9. Scanning electron photomicrographs of typical crack–particle interactions in Composite C.

in the alumina-rich regions of Composite C, toughening by the mechanism of frictional bridging will occur due to the presence of the 10% by volume of discrete iron particles. The corresponding alumina-rich regions in Composite B would not exhibit such a toughening mechanism. It was difficult, however, to observe and record plastic deformation of some of the larger iron agglomerations in Composite C. This was due to the reduced volume of agglomerated iron available for plastic deformation with Composite C in these cases. Under similar loading conditions, the plastic zone in a smaller volume of iron will neck to failure more quickly than with a large volume of iron.

It has already been suggested that the increase in fracture toughness of Composite B over that of Composite A is due to the energy dissipated on plastic deformation of large iron agglomerations. It would be expected, therefore, that the reduced amount of plastic deformation observed in Composite C when compared to Composite B would make Composite C less tough than Composite B. The fact that Composite C was tougher than Composite B highlights the need for a more

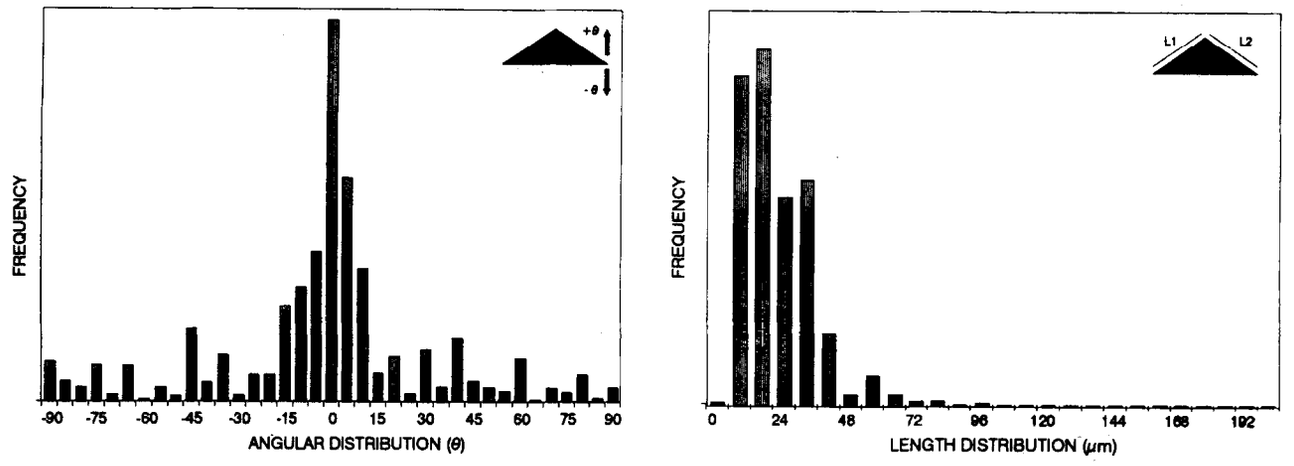

Fig. 10. Histograms depicting the length and angular distributions which describe the crack path in Composite C. Note each unit of length corresponds to 8 μm.

detailed examination of the toughening mechanisms. More information can be obtained by examination and interpretation of the crack profile of Composite C.

3.3.3 Crack path profile of Composite C

The histograms of angular and length distributions are shown in Fig. 10. Comparison of the angular distribution of Composite C with that of Composite B, shows that the shapes of these histograms are very similar. Whilst the most frequent angular distribution was between 0 and 5°, the deviations in the 10–45° region, as with Composite B, are likely to correspond to mechanical interlocking of the iron on the separation of the crack faces and frictional bridging.

If the length distribution histogram of Composite C is compared with that of Composite B, it can be seen that the shapes of these curves are different. Composite C has more lengths in the 192–256 μm region and does not contain as many lengths above 448 μm. The abundance of short lengths is related directly to the interactions with the discrete particles present in Composite C. This is the main difference between the behaviours of Composites B and C. It suggests that the combination of plastic deformation of large agglomerations and frictional bridging of discrete particles in Composite C imparts synergistically a greater shielding mechanism than the dominant mechanism of plastic deformation observed in Composite B.

The fracture toughness results of Composite C can be discussed in a descriptive manner. The increase in toughness of Composite C over that of Composite B can be explained by reference to Fig. 11. The large iron particles, with which interaction occurs on their central plane, are assumed to be mechanically interlocked and will therefore shield the crack tip by deforming plastically on crack opening. Large particles which are interacted with non-centrally, and all small particles, are assumed to shield via frictional bridging. All the lightly shaded particles are shielding the crack tip and the dark particles are no longer contributing to crack tip shielding.

The differences in Composite C when compared to Composite B are:

(i) The large particles in Composite B are larger than the equivalent large particles in Composite C.
(ii) Failure of the larger particles in Composite C occurs at smaller crack opening displacements than with Composite B and, therefore, the shielding term due to plastic deformation is lower in Composite C than in Composite B.
(iii) The small particles in between the larger particles of Composite C are all contributing to shielding whereas the matrix material in between the particles in Composite B does not have an associated shielding term.

It is suggested that the plastic deformation and debonding shielding mechanisms are acting synergistically in Composites B and C, but that the cumulative effect of the shielding in Composite C is greater than in Composite B. This accounts for the higher fracture toughness of Composite C when compared to Composite B. Hence, by assessing the toughening mechanisms which occur during a DCB test, the collated data can be used effectively to infer the changes required in the microstructure in order to maximise the fracture toughness.

4 Conclusions

The effects of changes in the distribution of 20% by volume of iron throughout alumina matrices

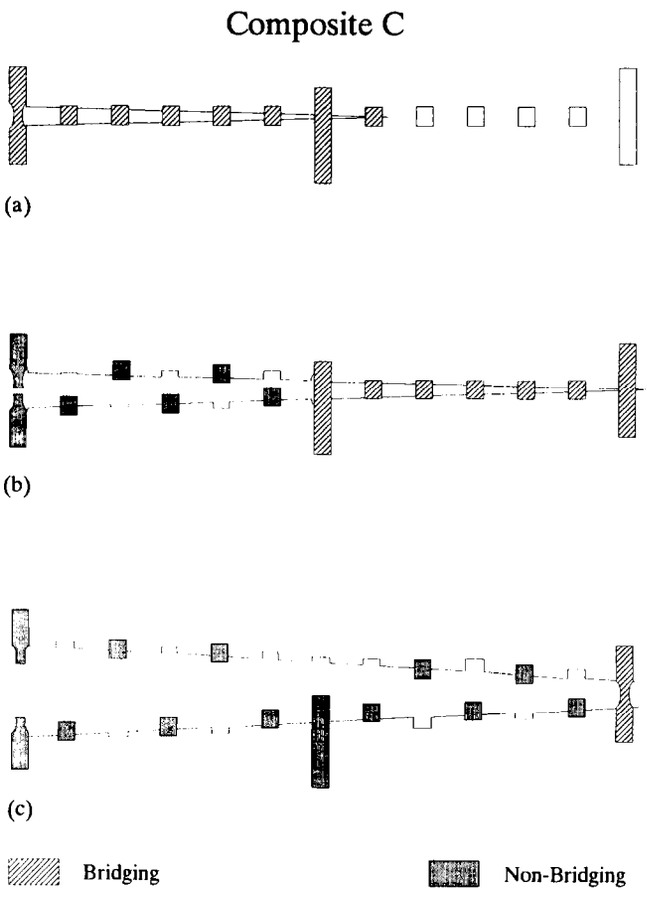

Fig. 11. Schematic illustration of the formation of bridging zones for a propagating crack in Composite C (open grains denote potential bridges, shaded grains denote active bridges and dark grains denote disengaged bridges): (a) crack intersects with many grains and shielding occurs via plastic deformation and frictional bridging; (b) the first set of grains disengage, the crack intersects with the next series of grains and bridges in the same manner as in (a); (c) the process zone.

on the propagation path of cracks through the material have been investigated. For all the composites studied, a tougher material than the monolithic alumina was produced. Control of the fabrication process from the powder processing stage has been shown to be the most important factor in producing different microstructures.

Two Composites, A and B, were compared and a greater understanding of the behaviour of these materials as cracks interact with them has been gained through the *in situ* nature of the fracture toughness testing technique. This knowledge can be used to predict the behaviour, as regards energy-dissipating mechanisms, of composites which have a specific distribution of ductile phase within a brittle matrix.

With Composite A, which contained a discrete dispersion of iron particles throughout an alumina matrix, the energy-dissipating mechanism observed was that of crack deflection. With Composite B, the larger iron agglomerations present in a 'honeycomb' distribution, dissipated energy both by crack deflection (70% of the iron) and plastic deformation (30% of the iron). The plastically deforming iron behaved like a hinge bridging the separating crack faces and this mechanism is different to that assumed in current modelling approaches. This information was used to produce a third composite, Composite C, which was the toughest of the three composites and exhibited the toughening mechanisms observed in both Composites A and B.

Acknowledgements

One of the authors (PAT) would like to acknowledge SERC for the provision of a Quota Award. The interest and support of colleagues at the University of Surrey is gratefully acknowledged.

References

1. Ashby, M. F., Blunt, F. J. & Bannister, M., Flow characteristics of highly constrained metal wires. *Acta Metall.*, **37** (1989) 1847.
2. Krstic, V. V., Nicholson, P. S. & Hoagland, R. G., Toughening of glasses by metallic particles. *J. Amer. Ceram. Soc.*, **64** (1981) 499.
3. Flinn, B. D., Rühle, M. & Evans, A. G., Toughening in composites of Al_2O_3 reinforced with Al. *Acta Metall.*, **37** (1989) 3001.
4. Sun, X., Trusty, P. A., Yeomans, J. A. & Shercliff, H. R., The fabrication and properties of alumina–ductile metal particle composites. In *Proceedings of ICCM8*, ed. S. W. Tsai & G. S. Springer. SAMPE, Hawaii, 1991. Paper 17J.
5. Tuan, W. H. & Brook, R. J., The toughening of alumina with nickel inclusions. *J. Euro. Ceram. Soc.*, **6** (1990) 31.
6. Trusty, P. A. & Yeomans, J. A., Crack–particle interactions in alumina–iron composites. *Ceram. Eng. Sci. Proc.*, **14** (1993) 908.
7. Budiansky, B., Amazigo, J. C. & Evans, A. G., Small-scale crack bridging and the fracture toughness of particulate-reinforced ceramics. *J. Mech. Phys. Solids*, **36** (1988) 167.
8. Mataga P. A., Deformation of crack-bridging ductile reinforcements in toughened brittle materials. *Acta. Metall.*, **37** (1989) 3349.
9. Hom, C. L., Mataga, P. A. & McMeeking, R. M., Some recent developments in numerical modelling of fracture toughness in brittle matrix composites. *Int. J. Num. Methods*, **27** (1989) 233.
10. Hing, P. & Grove, G. W., The strength and fracture toughness of polycrystalline magnesium oxide containing metallic particles and fibres. *J. Mater. Sci.*, **7** (1972) 427.
11. Sigl, L. S. & Fischmeister, H. F., On the fracture toughness of cemented carbides. *Acta Metall.*, **36** (1988) 887.
12. Xiao, L. S., Kim, Y. S., Abbaschian, R. & Hecht, R. J., Processing and mechanical properties of niobium-reinforced $MoSi_2$ composites. *Mater. Sci. Eng.*, **A144** (1991) 277.
13. Khaund, A. K., Krstic, V. D. & Nicholson, P. S., Influence of elastic and thermal mismatch on the local crack-driving force in brittle composites. *J. Mater. Sci.*, **12** (1977) 2269.
14. Tuan, W. H. & Brook, R. J., Processing of alumina/nickel composites. *J. Euro. Ceram. Soc.*, **10** (1992) 95.

15. Buljan, S., Pasto, S. & Kim, H. J., Ceramic whisker- and particulate-composites: Properties, reliability and applications. *J. Amer. Ceram. Soc.*, **68** (1989) 387.
16. Faber, K. T. & Evans. A. G., Crack deflection processes — 1. Theory. *Acta Metall.*, **31** (1983) 565.
17. Faber, K. T. & Evans. A. G., Crack deflection processes — 2. Experiment. *Acta Metall.*, **31** (1983) 577.
18. Mostovoy, S., Crosley, P. B. & Ripling, E. J., Use of crack-line-loaded specimens for measuring plain-strain fracture toughness. *Journal Materials*, **2** (1967) 661.
19. Trusty, P. A., The influence of microstructure on the fracture toughness of alumina-iron ceramic matrix composites. PhD thesis, The University of Surrey, UK, 1994.
20. Rôdel, J., Kelly, J. F. & Lawn, B. R., In-situ observations of toughening processes in alumina reinforced with silicon carbide whiskers. *J. Amer. Ceram. Soc.*, **74** (1991) 3154.
21. Vekinis, G., Ashby, M. F. & Beaumont, P. W. R., R-curve behaviour of Al_2O_3 ceramics. *Acta Metall.*, **38** (1990) 1151.
22. Shaw, L. & Abbaschian, R., Toughening $MoSi_2$ with niobium metal — effects of morphology of ductile reinforcements. *J. Mater. Sci.*, **30** (1995) 849.
23. Shercliff, H. R., Vekinis, G., Ashby, M. F. & Beaumont, P. W. R., United States Air Force Report, Grant No. AFOSR-87-0307 (1992).